University of Tehran Press

Online ISSN: 2345-475X

DESERT

Home page: https://jdesert.ut.ac.ir/

A Comparative Analysis of Feed-Forward and Long Short-Term Memory Networks for Solar Radiation Estimation

Soheila Mohtashami[1], Zahra Aghashariatmadari[1*]

[1] Department of Irrigation & Reclamation Engineering, University of Tehran, Karaj, Alborz Iran.
Email: zagha@ut.ac.ir

Article Info.

Article type:
Research Article

Article history:
Received: 15 Oct. 2025
Received in revised from: 18 Dec. 2025
Accepted: 24 Dec. 2025
Published online: 27 Dec. 2025

Keywords:
Solar radiation,
Artificial Neural Network,
Long Short-Term Memory,
Feed-Forward Neural Network,
Machine Learning Models.

ABSTRACT

Accurate estimation of solar radiation is essential for numerous industrial applications, energy management, and agricultural planning. This study investigates the effectiveness of advanced machine learning models for solar radiation prediction in Kerman Province, Iran, utilizing a comprehensive set of meteorological variables. Following rigorous quality control procedures and correlation-based feature selection, the dataset was divided into training (80%) and testing (20%) subsets. Two Neural Networks, namely Long Short-Term Memory (LSTM) with the Adam optimizer and Feed-Forward Neural Network (FFNN), were developed and trained under six input scenarios, employing various learning algorithms including Levenberg–Marquardt (LM), Bayesian Regularization (BR), Gradient Descent (GD), and Resilient Propagation (RP) at both daily and monthly timescales. The results indicate that the FFNN-BR model under scenario 6, incorporating a wide range of meteorological inputs, yielded the highest accuracy for monthly radiation estimation (R^2 = 0.92, ARE = 4.5%). For daily radiation prediction, the LSTM model under scenario 4 provided superior performance (R^2 = 0.91, ARE = 1.35%). These findings underscore the importance of model selection and input configuration in enhancing solar radiation estimation accuracy, offering valuable insights for renewable energy resource assessment in arid regions.

Cite this article: Mohtashami, S., Aghashariatmadari, Z. (2025). A Comparative Analysis of Feed-Forward and Long Short-Term Memory Networks for Solar Radiation Estimation. DESERT, 30 (2), DOI: 10.22059/jdesert.2025.106182

DOI: 10.22059/jdesert.2025.106182

Publisher: University of Tehran Press

1. Introduction

Renewable energy, with particular emphasis on solar energy, is widely recognized as an important source of energy at the global scale (Tazik *et al*., 2017; Afshari Pour *et al*., 2017). Solar radiation analysis and estimation are fundamental to a broad range of applications, including renewable energy production, environmental monitoring, agricultural optimization, and climate resilience planning (Wang *et al*., 2025; Zerouali *et al*., 2025). Moreover, solar radiation plays a critical role in sectors such as public health, electricity generation, tourism, and agriculture, all of which rely heavily on stable and sustainable energy systems (Wild, 2009; Asaf *et al*., 2013; Attya *et al*., 2025; Ghaffarzadeh & Azadian, 2019). Solar radiation directly influences various natural phenomena such as photosynthesis, temperature, evapotranspiration, and humidity (Gueymard & Myers, 2008). It also serves as a vital input for models that forecast the growth, development, and performance of agricultural products (Abraha & Savage, 2008).

The rapid growth of the global population has intensified energy demand worldwide, amplifying the urgency for clean and renewable energy sources (Meenal & Selvakumar, 2017; Bouat *et al*., 2018). In this context, solar energy has gained increasing attention due to its sustainability, abundance, and environmental compatibility. However, the effective utilization and planning of solar energy systems critically depend on the availability of accurate and reliable solar radiation data. Direct measurement using instruments such as pyranometers and pyrheliometers is considered the most accurate method for quantifying solar radiation (Oliveira *et al*., 2024). Despite their precision, these measurement systems face significant limitations, including high installation and maintenance costs, the need for skilled personnel, sparse spatial coverage, and potential data loss due to instrument malfunction (Ertekin & Yaldız, 1999; Zeng & Qiao, 2011; Shamshirband *et al*., 2015). As a result, many regions—particularly in developing, arid, and semi-arid areas—suffer from insufficient or incomplete solar radiation records.

To address these limitations, indirect estimation methods based on meteorological variables have been widely explored. Traditional empirical models have been developed to estimate solar radiation; however, their performance is often constrained by location-specific and season-dependent empirical coefficients, limiting their generalizability and necessitating recalibration when applied to new regions (Besharat *et al*., 2013). In recent years, Artificial Intelligence (AI)–based models have emerged as powerful alternatives, capable of capturing nonlinear relationships between solar radiation and meteorological inputs while reducing reliance on extensive measurement infrastructure (Yan *et al*., 2025).

An increasing number of studies have demonstrated the effectiveness of AI techniques for solar radiation prediction and estimation (Tilahun, 2024; Wang *et al*., 2025; Zerouali *et al*., 2025; Yan *et al*., 2025; Cervantes *et al*., 2025; Yadav *et al*., 2025; Arseven & Cınar, 2025; Rai *et al*., 2025). Various data-driven approaches—including artificial neural networks (ANNs), genetic algorithms, fuzzy logic systems, and hybrid models—have been applied across different climatic zones, temporal resolutions, and input configurations (Camacho *et al*., 2012; Yadav, Chandel, 2014). Qazi *et al*. (2015) showed that ANN-based models could predict solar radiation with errors below 20%. Abdulazeez (2011) employed a Feed-Forward Backpropagation Neural Network using sunshine duration, maximum temperature, and relative humidity as inputs, achieving a low RMSE of 0.0028. More recent studies have expanded the scope of machine learning techniques, such as Random Forest, XGBoost, and deep learning models. Venkata Teja *et al*. (2025) reported superior performance of XGBoost over Random Forest, while Demir (2025) demonstrated the effectiveness of LSTM and Bi-LSTM models using NASA/POWER

data. Kusuma *et al*. (2025) further improved prediction accuracy by integrating decomposition techniques with Feed-Forward Neural Networks, achieving an MAE of 3.38 and a MAPE of 0.29%. Collectively, these studies confirm that supervised learning approaches are highly effective for solar radiation estimation and adaptable across diverse climatic conditions.

Despite these advancements, several gaps remain in the existing literature. First, most previous studies focus on a single temporal resolution, typically daily or monthly, limiting the understanding of model performance across multiple time scales. Second, limited attention has been given to systematic comparisons between time step–dependent models (e.g., LSTM) and time step–independent models (e.g., FFNN) under identical climatic and data conditions. Third, although FFNNs have been widely used, most studies rely primarily on the Bayesian Regularization (BR) and Levenberg–Marquardt (LM) learning algorithms, with relatively little exploration of alternative training algorithms (Lauret *et al*., 2006; Yacef *et al*., 2012; Waewsak *et al*., 2014; Mazorra Aguiar *et al*., 2015; Jazayeri *et al*., 2016; Celik *et al*., 2016; Hari & Subbulekshmi, 2022; Malik *et al*., 2023;). Finally, few studies explicitly address arid and semi-arid regions, despite their high dependence on solar radiation for energy and agricultural sustainability (Gürel *et al*., 2023; Adam *et al*., 2025).

To address these gaps, this study focuses on an arid/semi-arid region and conducts a comprehensive comparison of Feed-Forward Neural Networks (FFNNs) and Long Short-Term Memory (LSTM) networks for solar radiation estimation at both daily and monthly time scales. The specific objectives of this research are to:

evaluate and compare the performance of a time step–dependent model (LSTM) and a time step–independent model (FFNN) across two temporal resolutions;

investigate the impact of four distinct learning algorithms on FFNN performance beyond the commonly used BR and LM methods;

assess the influence of data quality control and meteorological variable correlations at daily and monthly scales; and

identify the most suitable modeling approach for accurate solar radiation estimation in the selected study area.

The results of this study enhance the understanding of AI-based approaches for solar radiation modeling and offer practical insights for model selection in data-scarce arid and semi-arid regions.

2. Materials and methods

2.1 Study Area

Kerman province, located in the southeastern region of Iran, holds the distinction of being the largest province in the country, encompassing approximately 11% of Iran's total land area, spanning across 183,285 square kilometers. Geographically, it lies between 56° 19' to 57° 25' East longitude and 30° 2' to 30° 28' North latitude. The province’s elevation ranges from 1,605 to 2,076 meters above sea level. Notably, the average temperature on the plains is recorded at 15.8°C, accompanied by an annual rainfall of 132.73 millimeters. Figure 1 illustrates the geographical location of the location of Kerman province. Meteorological data have been collected from this station starting from January 2015, continuing until November 2023.

2.2. Validation and quality control of radiation data

Accurate and reliable radiation observational data is of utmost importance (Bian *et al*., 2019). In order to achieve this, the study utilized Moradi's algorithm for radiation data quality control

(Moradi, 2009). The quality control process consists of three stages to ensure the accuracy and reliability of radiation observational data, as follows:

2.2.1. Comparing Global Daily Solar Radiation with Extraterrestrial Daily Radiation

In the first step, the global daily solar radiation (R_s) is compared with the extraterrestrial daily radiation (R_0) received at the horizontal surface outside the Earth's atmosphere. The comparison is made using Equation (1) (Moradi, 2009):

$$0.03R_0 \le R_s < R_0 \tag{1}$$

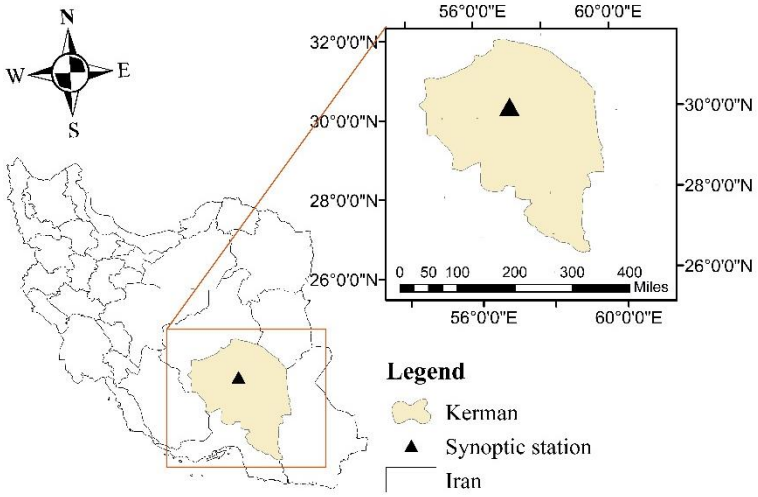

Fig. 1. The study area and the location of Kerman synoptic station

2.2.2. Limiting Daily Solar Radiation with Clear Sky Radiation

The second step involves ensuring that the observed solar radiation (R_s) does not exceed a certain threshold represented by the small amount of daily clear sky radiation (R_{cd}) observed under very clear sky conditions. Equation (2) defines this condition (Moradi, 2009):

$$R_s < 1.1R_{cd} \tag{2}$$

2.2.3. Checking Radiation Stability using the Radiation Index

The third stage consists of stability checks that utilize the relationship between daily global solar radiation and the sunshine hours fraction. In this step, a new index called the radiation index (i_n) is calculated and compared to its lowest limit (LL) using Equation (3) (Moradi, 2009). The radiation index takes into account the atmospheric clearness index (K_T), which is the ratio of observed solar radiation (R_s) to extraterrestrial radiation (R_0), and the sunshine hours fraction (N_n).

$$i_n = \begin{cases} K_T & if \ \ n < 0.05 \ or \ \ K_T < 0.1 \\ \dfrac{K_T}{N_n} & else \end{cases} \tag{3}$$

The lower limit of the index is determined using Equation (4), which incorporates several

parameters: parameter a, representing the second quartile (median) of K_T for all days where the sunshine hours fraction (n/N) exceeds 0.9; parameter b, representing the first quartile of data with n/N values less than or equal to 0.1; and parameter c, which is the ratio n/N (Moradi, 2009).

$$i_n = \begin{cases} a\dfrac{n}{N} & if\ \dfrac{n}{N} \geq c \\ b & else \end{cases} \quad (4)$$

Overall, these three stages provide a comprehensive approach to quality control for radiation data, ensuring that the observed values are consistent with the expected ranges and relationships. To ensure data quality, outlier detection and removal were performed on the daily radiation measurements from 2015 to 2023. Approximately 1.7% of the observations were identified as outliers and removed, ensuring the reliability of the dataset for further analysis.

2.3. Feature Selection

To introduce ANNs and determine the suitable input features for it, Pearson correlation was utilized to calculate the correlation between radiation and meteorological variables based on Equation (5). Where, COV represents the covariance, σ_x denotes the standard deviation of a meteorological variable, and σ_y represents the standard deviation of the solar radiation data (Benesty *et al*., 2008; Edelmann *et al*., 2021). Correlation calculations were performed at both daily and monthly scales, allowing the identification of correlation values. These values are crucial for selecting the appropriate variables as inputs to the ANNs and for defining the scenarios. Correlations were computed using the "corr" function available in MATLAB software.

$$\rho_{x,y} = \frac{COV(X,Y)}{\sigma_x \sigma_y} \quad (5)$$

2.4. ANN development

ANNs are powerful tool within the field of AI that serves various purposes such as nonlinear function estimation, data classification, pattern recognition, optimization, clustering, and simulation. The structure of an ANN consists of several components, including the input layer, hidden layer(s), output layer, weights, biases, activation functions, and neurons. During the training phase, the network utilizes these weights and biases to minimize the error function and generate the desired output. The learning process involves the application of specific algorithms and training procedures (Yadav & Chandel, 2014). In this research, FFNN was employed to develop the model. The FFNN architecture will be introduced further in subsequent sections. Additionally, the research proposes an estimating method for radiation based on LSTM techniques. LSTM, known for its ability to analyze relationships in time series data through its memory function, enhances the model's capabilities in capturing temporal patterns and dependencies.

2.4.1. FFNN

FFNNs hold a significant position among ANNs due to its distinctive structure devoid of cycles or loops (Bohat & Arya, 2018). The FFNN architecture comprises an input layer connected to a hidden layer, and it is common for ANNs to have only one hidden layer, with rare instances of networks having more than two hidden layers (Heaton, 2008). In FFNN, the connections between neurons are unidirectional and established through weights. Figure 2 illustrates a simple FFNN

structure with one hidden layer. Where m represents the number of inputs, n denotes the number of neurons in the hidden layer, and O signifies the output. The FFNN's operation involves calculating the weighted sum of inputs to a node, followed by the application of an activation function. Various activation functions exist, but the sigmoid function is widely utilized and popular (Bohat & Arya, 2018). In this study, the sigmoid function was selected as the activation function. Mathematically, the process can be represented as Equation (6) (Okut, 2016), where f_k denotes the activation function, I_m represents a vector of inputs (independent variables), b_m signifies the bias vector, and W_{mn} represents the connected weight between input m and hidden layer n.

$$H_n = f_k\left(b_n + \sum_{m=1}^{m} w_{mn} I_m\right) \tag{6}$$

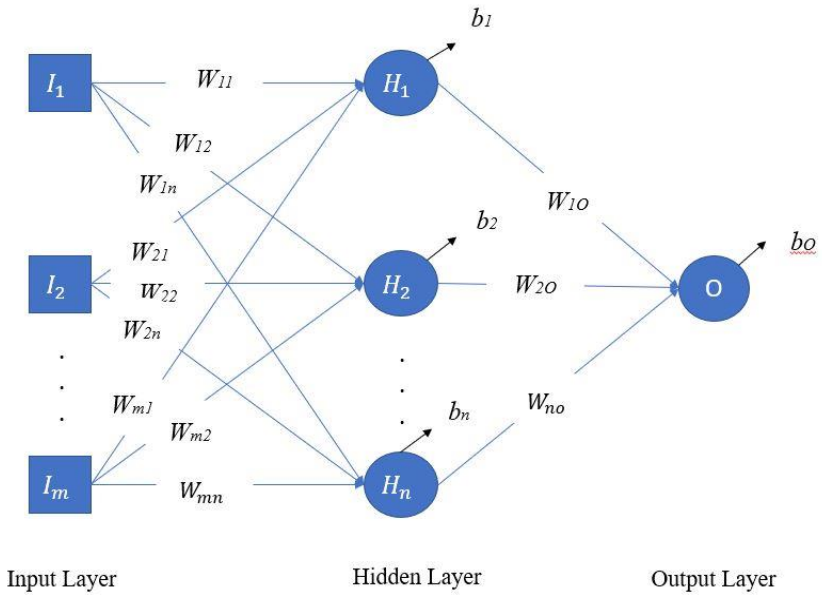

Fig. 2. A simple architecture of FFNN

The key advance is the introduction of a learning algorithm, which finds the weight and offset parameters of the network for a particular problem (Bohat & Arya, 2018). In this study, four learning algorithms were selected to train FFNN, including Bayesian Regularization (BR), Levenberg-Marquardt (LM), Resilient Back-propagation (RP), and Gradient Descent (GD). A brief description of these algorithms is given in the following subsections.

The BR learning algorithm: The BR algorithm uses Bayes' rule to update the weights of the ANN and mitigate overfitting. The cost function (CF) for the BR learning algorithm is defined by Equation (7). Where n represents the number of input data, m represents the number of neurons in the output layer, Δ_{ij}, α, and β is determined by Equation (8), Equation (9), and Equation (10), respectively. T_{ij} represents the network target and O_{ij} denotes the network output for a given input i and neuron j of the output layer.

$$F = CF_{SD} + \beta \sum_{K=1}^{p}\sum_{l=1}^{q} \quad , \quad CF_{SD} = \alpha \sum_{i=1}^{n}\sum_{j=1}^{m} \Delta_{ij}^2 \tag{7}$$

$$\triangle_{ij} = T_{ij} - O_{ij} \tag{8}$$

In the Equation (9) and (10), m represents the maximum posterior, and γ corresponds to the number of parameters that have a greater relative impact on reducing the CF value. W_{Kl} denotes the weight between neurons k and l.

$$\alpha = \frac{n-\gamma}{2\sum_{i=1}^{n}\sum_{j=1}^{m}\triangle_{ij}^{2}\left(w^{M}\right)} \tag{9}$$

$$\beta = \frac{\gamma}{2\sum_{k=1}^{P}\sum_{l=1}^{q}w_{kl}^{2}\left(w^{M}\right)} \tag{10}$$

The distribution of weights follows a Gaussian function, as expressed in Equation (11). Where P represents the probability function, W represents the weights vector, and P represents the input data vector (Moshkbar-Bakhshayesh, 2021).

$$\mathrm{P}(W \mid P,\ \alpha,\beta) = \frac{\mathrm{P}\left(P \mid W,\alpha\right)\mathrm{P}(W \mid \beta)}{\sum \mathrm{P}\left(P \mid W,\alpha\right)\mathrm{P}(W \mid \beta)\Delta W} \tag{11}$$

The LM learning algorithm: The weights of the FFNN are typically updated using the steepest descent (SD) algorithm, as shown in Equation (12). However, the SD algorithm has a relatively slow convergence rate. To address this, a stable and fast learning algorithm called the Levenberg-Marquardt (LM) algorithm is employed by combining the Gauss-Newton (GN) method with the SD algorithm, as presented in Equation (13). The GN method is defined by Equation (14), where J represents the Jacobian matrix, E represents the error matrix, and I represent the identity matrix (Moshkbar-Bakhshayesh, 2021). LM algorithm behaves akin to gradient descent, while for lesser values, it resembles GaussNewton. By combining the strengths of "GaussNewton" and gradient descent approaches, the LM algorithm effectively addresses the given problem (Chauhan *et al*., 2024).

$$\Delta w_{ij} = \frac{\partial CF_{SD}}{\partial w_{ij}} \tag{12}$$

$$\Delta w_{LM} = \Delta w_{GN} + \left(\frac{1}{\alpha} I\right)^{-1} JE \tag{13}$$

$$\Delta w_{GN} = \left(J^{T} J\right)^{-1} JE \tag{14}$$

The GD learning algorithm: The core principle of the Gradient Descent (GD) learning algorithm involves iteratively updating the dynamic parameters in the direction opposite to the gradient of the error (E), aiming to minimize this discrepancy. This update process is described by Equation (15), where μ represents the learning rate, w denotes the weight of the neuron, and b signifies the bias (Moshkbar-Bakhshayesh, 2019).

$$\Delta w = -\mu \frac{\partial E}{\partial w}, \Delta b = -\mu \frac{\partial E}{\partial b} \tag{15}$$

The RP learning algorithm: The RP algorithm is an enhanced version of the traditional batch back-propagation algorithms, known for its fast convergence for many problems. It offers rapid local adaptation by utilizing only the sign of the back-propagated gradient to update the

network's biases and weights, rather than considering the magnitude of the gradient itself. In other words, the direction of the weight/bias update is determined solely by the sign of the derivative. The weight adjustments are made according to Equation (16) and Equation (17) (Yang *et al*., 2016; James *et al*., 2018; Reddy *et al*., 2020). The values $0 < \mu^- < 1 < \mu+$ are empirically set as 0.5 and 1.2, respectively.

$$\Delta_{ij}(t) = \begin{cases} \mu^+ . \Delta_{ij}(t-1), & if \ \frac{\partial E}{\partial w_{ij}}(t-1) . \frac{\partial E}{\partial w_{ij}}(t) > 0 \\ \mu^- . \Delta_{ij}(t-1), & if \ \frac{\partial E}{\partial w_{ij}}(t-1) . \frac{\partial E}{\partial w_{ij}}(t) < 0 \\ \Delta_{ij}(t-1), & otherwise \end{cases} \tag{16}$$

$$w_{ij}(t) = \begin{cases} -\Delta_{ij}(t), & if \ \frac{\partial E}{\partial w_{ij}}(t) > 0 \\ +\Delta_{ij}(t), & if \ \frac{\partial E}{\partial w_{ij}}(t) < 0 \\ 0, & otherwise \end{cases} \tag{17}$$

The weight update process in the RP algorithm can be summarized as follows: When the partial derivative of the error function (E) with respect to a specific weight wij changes its sign, it indicates that the previous update was too large, causing the algorithm to overshoot a local minimum. In such cases, the updated value is decreased by a certain factor. Conversely, if the derivative maintains its sign, the updated value is slightly increased by the factor to facilitate faster convergence in shallow regions. Once the updated values for all weights are adjusted, the weight update itself adheres to a straightforward rule: If the derivative is positive (indicating an increasing error), the weight is decreased by its update value. Conversely, if the derivative is negative, the update value is added to the weight (Yang *et al*., 2016).

2.4.2. LSTM

LSTM is a variant of the Recurrent Neural Network (RNN) that incorporates additional components such as a cell, input gate, output gate, and forget gate (Hochreiter & Schmidhuber, 1997; Pan *et al*., 2023). This architecture enables an LSTM layer to effectively capture long-term dependencies, making it particularly suitable for time-series prediction tasks. In a typical configuration, an LSTM layer consists of multiple LSTM cells and a dense output layer. Figure 3 depicts the fundamental structure of an LSTM cell, comprising three key gates: the input gate (i_t), forget gate f_t, and output gate O_t, along with the candidate value C_t at each time step (Fischer & Krauss, 2018). The relationships between these gates are mathematically defined by the following Equations (28).

$$f_t = \alpha\left(w_{i,x}.x_t + w_{i,h}.h_{t-1} + b_i\right) \tag{18}$$

$$i_t = \alpha\left(w_{f,x}.x_t + w_{f,h}.h_{t-1} + b_f\right) \tag{19}$$

$$o_t = \alpha\left(w_{o,x}.x_t + w_{o,h}.h_{t-1} + b_o\right) \tag{20}$$

$$\hat{C}_t = tanh\left(w_{\hat{c},x}.x_t + w_{\hat{c},h}.h_{t-1} + b_{\hat{c}}\right) \tag{21}$$

In the LSTM architecture, there are weight matrices denoted as $w_{(i,x)}$, $w_{(i,h)}$, $w_{(f,x)}$, $w_{(f,h)}$,

$w_{(o,x)}$, $w_{(o,h)}$, $w_{(c,x)}$ and $w_{(c,h)}$. These weight matrices consist of parameters ranging from 0 to 1. A parameter value closer to 1 implies that more information is retained, with 1 indicating complete preservation and 0 indicating complete forgetting. Additionally, there are bias vectors b_i, b_f, b_o and b_c. The current input is represented by x_t, the output of the LSTM at the previous time is denoted as $h_{(t-1)}$, and α denotes the activation function. The forget gate determines the amount of prior memory value to be discarded from the cell state, while the input gate determines the new input to be added to the cell state. Finally, the cell state c_t is calculated as the Equation (Okut, 2016):

$$c_t = f_t * c_{t-1} + i_t * \hat{c}_t \tag{22}$$

The output h_t of the LSTM at the time t is derived as Equation (23):

$$h_t = O_t * tanh(C_t) \tag{23}$$

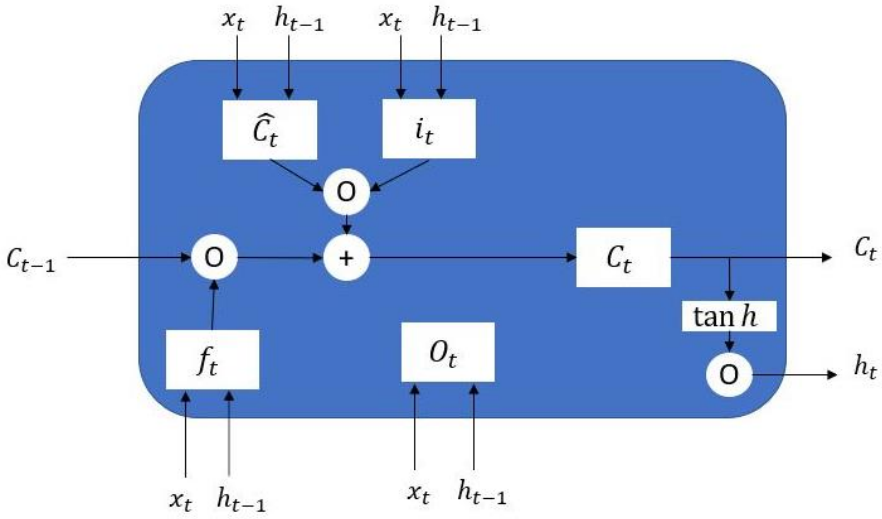

Fig. 3. The schematic structure of an LSTM cell

In this study, a single-layer LSTM architecture was utilized with the number of neurons determined in proportionally to the number of inputs, as indicated in Table 3. To update the parameters of the LSTM model, the Adam optimizer was used, which is well known in the field of deep learning for its self-adaptive learning rate and fast convergence speed. 80% of the dataset was used for training and 20% as a test dataset.

2.5 Model evaluation

To assess the performance and reliability of the developed models, several error evaluation criteria were utilized, including MAE (Mean Absolute Error), RMSE (Root Mean Squared Error), MBE (Mean Bias Error), ARE (Absolute Relative Error), and R^2 (R-square). The equations for these evaluation metrics are provided in Table 1. In the Equations (24) to (28), O_i represents the observed values, X_i is the estimated values, N represents the number of data points, RSS represents the sum of squares of residuals, and TSS represents the total sum of squares.

Table 1. Error evaluation criteria and their relationship

Formula	Number of Equation
$MAE = \frac{1}{N}\sum_{i=1}^{N}\lvert X_i - O_i\rvert$	(24)
$RMSE = \sqrt{\frac{1}{N}\sum_{i=1}^{N}(X_i - O_i)^2}$	(25)
$MBE = \frac{1}{N}\sum_{i=1}^{N}(X_i - O_i)$	(26)
$ARE = \frac{1}{N}\sum_{i=1}^{N}\frac{X_i - O_i}{O_i}\times 100$	(27)
$R^2 = 1 - \frac{RSS}{TSS}$	(28)

Figure 4 shows a flowchart of the research steps. Initially, solar radiation and meteorological data were collected and subjected to a three-stage quality control using Moradi's algorithm (Moradi, 2009). Pearson's correlation coefficient, as a widely used metric to evaluate relationships between variables (Benkaciali *et al*., 2025), was employed for feature selection and scenario construction. Two Neural Networks were developed: a FFNN with a single hidden layer and sigmoid activation trained using four algorithms (BR, LM, GD, RP), and a single-layer LSTM to capture temporal dependencies, trained with the Adam optimizer. Model performance was evaluated using MAE, RMSE, MBE, ARE, and R^2 to ensure accuracy and reliability.

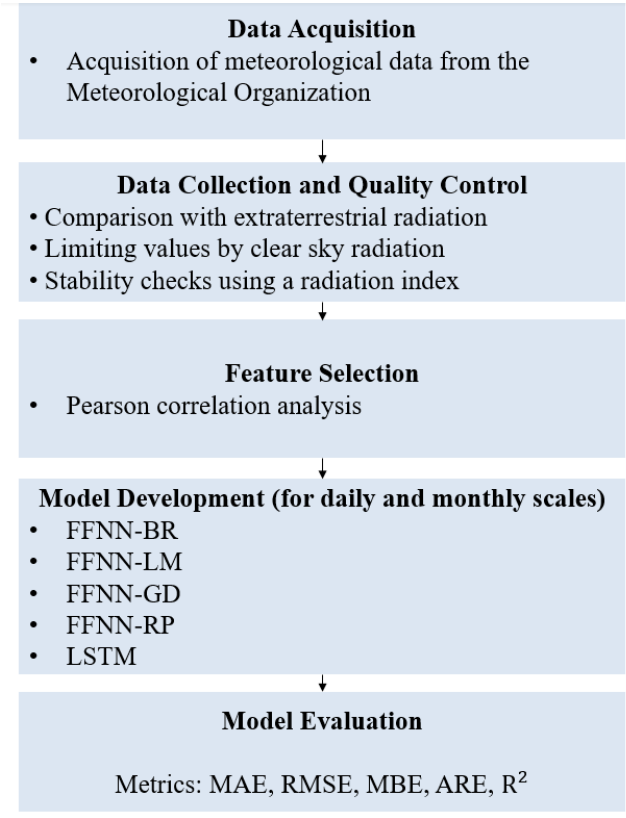

Fig. 4. Flowchart of the research steps

3. Results and discussion

3.1. Feature selection

The results of the correlations are presented in Table 2 and Figure 5. As shown in Table 2, the correlations tend to be stronger on a monthly scale compared to a daily scale. On a monthly scale, the highest correlation with radiation is observed for evaporation, while the lowest correlation is observed with the average dew point temperature. On a daily scale, the highest correlation with radiation is found with sunshine hours, whereas the lowest correlation is observed with maximum wind speed. Except for the average dew point temperature, all meteorological parameters exhibit similar correlations on both daily and monthly scales. Parameters such as average pressure, average vapor pressure, precipitation, average cloudiness, maximum cloudiness, maximum relative humidity, minimum relative humidity, average relative humidity, maximum pressure, minimum pressure, and dew point temperature exhibit a negative correlation with radiation on a daily scale.

A study conducted in Nigeria investigated the impact of relative humidity on solar radiation intensity, revealing that an increase in relative humidity leads to a decrease in solar radiation and vice versa (Tasie *et al*., 2018). These findings align with a study by Jebli *et al*. (2021) which explored the correlation between solar radiation and meteorological variables such as relative humidity, air pressure, temperature, and wind speed. Similarly, a study discovered strong correlations (greater than 0.5) between solar radiation and variables such as temperature, soil temperature, relative humidity, sunshine hours, and saturated vapor pressure (Fraihat *et al*., 2022). These results are consistent with the findings of the present study.

Table 2. Correlation between Rs and variables on daily scale and monthly scale

Parameter	Correlation on the monthly scales	Correlation on the daily scale
Horizontal visibility	0.2605	0.2589
Maximum wind speed	0.4261	0.0728
Mean wind speed	0.5801	0.1761
Maximum temperature	0.9225	0.7442
n/N	0.8700	0.9314
Minimum temperature	0.9140	0.5747
Mean temperature	0.9327	0.7230
Mean pressure	-0.7600	-0.4359
Mean vapor pressure	0.1861	-0.1622
Precipitation	-0.3850	-0.3095
Mean cloudiness	-0.5636	-0.5905
Maximum cloudiness	-0.5286	-0.5162
Maximum relative humidity	-0.8061	-0.6475
Minimum relative humidity	-0.7218	-0.6141
Mean relative humidity	-0.7983	-0.6857
Sunshine hours	0.8676	0.8005
Radiation	1	1
Evaporation	0.9441	0.6656
Dew point temperature	0.2218	-0.1142
Wet bulb temperature	0.8858	0.5715
Mean soil temperature	0.9107	0.5666
Minimum soil temperature	0.9107	0.5666
Maximum pressure	-0.7864	-0.4540
Minimum pressure	-0.7390	-0.4136
Saturated vapor pressure	0.9141	0.7177

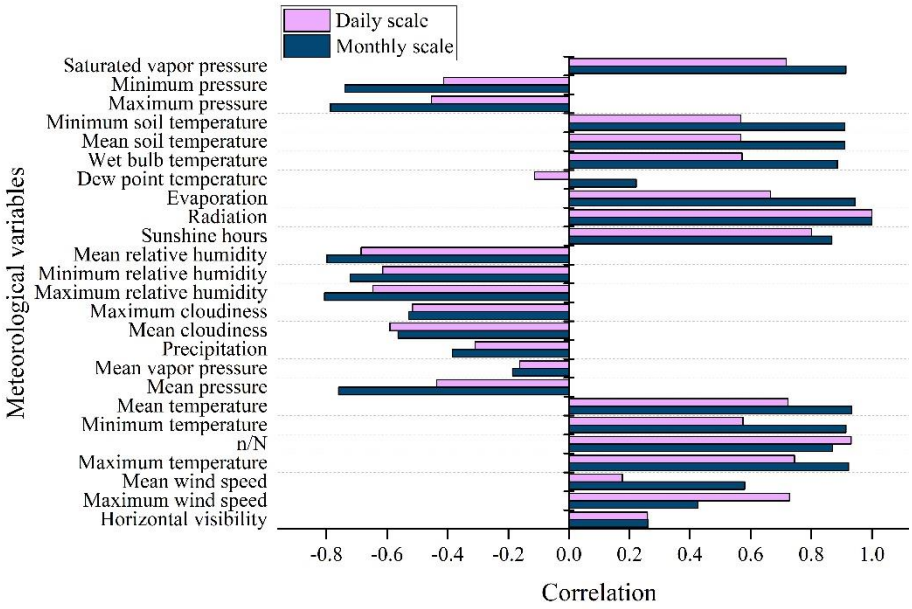

Fig. 5. Correlation between R_s and variables on daily and monthly scale

The study identified several variables that play a significant role in determining the amount of daily and monthly radiation. For the daily scale, the variables found to be influential were the fraction of sunshine hours (n / N), mean saturated vapor pressure, mean temperature, relative humidity, and mean soil temperature. For the monthly scale, the most important features were identified as mean temperature, mean saturated vapor pressure, soil temperature, sunshine hours, and relative humidity, respectively. Based on the degree of correlation, the selection of scenarios for ANNs was performed based on the information provided in Table 3.

As shown in Table 3, six scenarios were defined to investigate the effect of different input variables on model performance. Scenario 1 includes n/N; Scenario 2 includes n/N and SVP; Scenario 3 includes n/N, SVP, and MAT; Scenario 4 includes n/N, SVP, MAT, and MRH; Scenario 5 includes n/N, SVP, MAT, MRH, and MST; and Scenario 6 includes all remaining variables, including HV, MW, C, DP, WB, and P. The number of neurons in each scenario was adjusted according to the complexity of the inputs, ranging from 1 neuron in Scenario 1 to 10 neurons in Scenario 6. The number of neurons in the hidden layer was selected according to heuristic rules suggested in Heaton (2008).

Table 3. LSTM/FFNN scenarios and structure on the daily/monthly scale

Scenario	Number of neurons	Output	Inputs
1	1	R_S/R_0	n/N
2	2	R_S/R_0	n/N, SVP
3	3	R_S/R_0	n/N, SVP, MAT
4	4	R_S/R_0	n/N, SVP, MAT, MRH
5	4	R_S/R_0	n/N, SVP, MAT, MRH, MST
6	10	R_S/R_0	n/N, SVP, MAT, MRH, MST, HV, MW, C, DP, WB, P

3.2 Result of developing models

The models were evaluated across six scenarios with progressively increasing feature dimensionality and data complexity. Error metrics including RMSE, MAE, MBE, ARE, and R^2 were calculated for both training and testing datasets at daily and monthly scales.

Tables 4 and 5 summarize the training and testing errors of FFNN models using four learning algorithms (LM, BR, GD, and RP) across all scenarios. Similarly, Tables 6 and 7 report the corresponding errors for LSTM models. In the following sections, the performance of FFNNs under different learning algorithms is analyzed (Section 3.3), followed by scenario-based analysis of LSTM networks (Section 3.4), and a detailed comparison between FFNN and LSTM models at both daily and monthly scales (Sections 3.5 and 3.6).

3.3 Comparison of FFNNs under different learning algorithms

The six scenarios considered in this study were designed to progressively increase the number of input features, thereby introducing higher data complexity and richer information content. Accordingly, the observed differences in model performance across scenarios can be interpreted as reflecting the relative ability of the learning algorithms to utilize an expanded input space while maintaining generalization capability.

According to the findings in Table 4, the comparative analysis of the modeling errors across different training algorithms revealed significant variations in performance. Among the evaluated methods, the LM and BR algorithms consistently demonstrated superior accuracy. Both algorithms yielded the lowest RMSE and MAE values, along with relatively small MBE, indicating that their predictions were not systematically over/under-estimated. Furthermore, their R^2 values were generally above 0.87 and, in several scenarios, exceeded 0.90, confirming a strong correlation between the predicted and observed data. This indicates that LM and BR are more capable of capturing the nonlinear relationships inherent in solar radiation data across different scenario settings.

The performance of the RP algorithm was slightly weaker compared to LM and BR, yet still acceptable. RP maintained relatively low error indices and R^2 values close to 0.90 in most cases, suggesting it can be considered a reliable alternative when computational efficiency is prioritized. However, its slightly higher variability across scenarios indicates a lower robustness compared to LM and BR when scenario complexity increases.

In contrast, the GD algorithm performed poorly across all scenarios. Its RMSE and MAE values were significantly higher than those of the other methods, while the ARE reached values above 15% in some cases. Moreover, the R^2 values for GD were substantially lower, in certain scenarios dropping below 0.2, which indicates poor model fitting and weak predictive capability.

Another important observation is that the differences between training and testing errors vary across algorithms and scenarios. For LM and BR, these differences are generally small, indicating good generalization across all scenarios. RP shows moderate variability, while GD exhibits substantial differences in certain scenarios (e.g., Scenario 6 at both daily and monthly scales), reflecting poor generalization and unstable learning behavior. Therefore, the differences between training and testing errors should not be assumed negligible across all models, especially in higher-complexity scenarios.

Overall, the findings indicate that LM and BR are the most reliable algorithms for this modeling framework, with BR showing marginal advantages in terms of error reduction and R^2 improvement. RP can be considered a secondary option, whereas GD is unsuitable due to its low accuracy and poor correlation with the observed data.

A cross-scenario analysis revealed that the modeling performance improved progressively from Scenario 1 to Scenario 6. In the initial scenario, the accuracy of LM and BR was acceptable, with R^2 values around 0.87. However, as the scenarios advanced, both algorithms achieved higher accuracy, with R^2 values consistently exceeding 0.90 from Scenario 3 onward. This trend indicates that the models captured the underlying relationships more effectively in later scenarios, likely due to richer input information and improved data representation.

The RP algorithm exhibited a similar trend, though with slightly weaker results compared to LM and BR. Its R^2 values increased from approximately 0.86 in Scenario 1 to nearly 0.90 in Scenario 6, suggesting that RP also benefitted from the gradual improvement in scenario structure. On the contrary, the GD algorithm showed unstable and highly unreliable performance throughout the scenarios. In Scenarios 2 and 3, its predictive accuracy collapsed, with R^2 dropping below 0.40 and even 0.12, indicating severe divergence from the target values. Although Scenario 6 showed some improvement ($R^2 \approx 0.67$ in testing), GD still remained far less accurate than the other methods.

Another important observation is the systematic reduction in error indices across scenarios. For LM and BR, both RMSE and MAE decreased steadily, reaching their minimum values in Scenarios 5 and 6. This result highlights the robustness of these algorithms in handling increasingly complex or refined scenarios. RP followed the same decreasing error trend, whereas GD showed inconsistent and large error fluctuations, confirming its unsuitability for reliable scenario-based modeling.

Table 4. Training error and testing error for FFNN on the monthly scale

Information		Test					Train				
Scenario	Algorithm	RMSE	MAE	MBE	ARE	R^2	RMSE	MAE	MBE	ARE	R^2
1	LM	0.0020	0.0368	0.0027	5.939	0.8718	0.0021	0.0365	0.0120	6.0666	0.8739
	BR	0.0021	0.0368	0.0019	5.91	0.8718	0.0021	0.0364	0.0113	6.0092	0.8743
	GD	0.0025	0.04	0.0021	6.4747	0.8528	0.0024	0.039	0.0112	6.4973	0.8549
	RP	0.0023	0.0383	-0.0008	6.2549	0.8585	0.0023	0.0373	0.0081	6.3069	0.8622
2	LM	0.0015	0.0307	0.0009	5.0639	0.9037	0.0019	0.0332	0.0116	5.5771	0.8897
	BR	0.0015	0.0306	0.0006	5.0351	0.9042	0.0019	0.0332	0.0115	5.5543	0.8898
	GD	0.0113	0.0871	-0.0039	15.6181	0.3707	0.0115	0.0861	0.0107	15.7133	0.3653
	RP	0.0016	0.0313	0.0002	5.1693	0.9008	0.0019	0.0335	0.0104	5.6502	0.8874
3	LM	0.0015	0.0304	-0.0008	4.9874	0.9061	0.0018	0.0326	0.0108	5.4452	0.8943
	BR	0.0015	0.0305	-0.0008	4.9763	0.9063	0.0018	0.0325	0.0107	5.4202	0.8952
	GD	0.0173	0.099	-0.0102	18.0399	0.123	0.0172	0.0958	0.0187	17.957	0.1164
	RP	0.0015	0.0305	0.0001	4.9857	0.9066	0.0018	0.0328	0.0119	5.4699	0.8954
4	LM	0.0015	0.0302	0.0003	4.9656	0.9071	0.0017	0.0319	0.0111	5.3617	0.8992
	BR	0.0014	0.0297	-0.0005	4.8402	0.9107	0.0017	0.0321	0.011	5.3622	0.8984
	GD	0.0084	0.0695	0.0139	12.4382	0.4899	0.0123	0.0868	0.0253	15.2132	0.3034
	RP	0.0016	0.0314	0.0002	5.2248	0.8974	0.0018	0.0325	0.0102	5.5294	0.8931
5	LM	0.0015	0.0301	0.0005	4.9097	0.9083	0.0017	0.0321	0.0111	5.3367	0.899
	BR	0.0014	0.03	-0.0006	4.8589	0.9098	0.0017	0.0317	0.0102	5.2534	0.9007
	GD	0.0104	0.0786	-0.0002	13.5461	0.4139	0.0088	0.0704	0.007	12.7073	0.486
	RP	0.0016	0.0312	-0.0004	5.1395	0.8995	0.002	0.0344	0.0098	5.7848	0.8782
6	LM	0.0014	0.0294	-0.0032	4.7788	0.9127	0.0016	0.0306	0.0067	5.0899	0.9045
	BR	0.0013	0.0279	-0.0007	4.5406	0.919	0.0015	0.0299	0.0094	4.9118	0.9113
	GD	0.0056	0.0564	0.0053	9.2974	0.6754	0.0071	0.0663	0.0066	10.799	0.6228
	RP	0.0016	0.0308	-0.0005	5.0917	0.8988	0.0019	0.0335	0.0113	5.6144	0.8875

In summary, the scenario-based analysis indicates that Scenarios 5 and 6 provided the most accurate and stable results, particularly when using LM and BR algorithms. These findings suggest that the data structure and feature composition in these scenarios were more favorable for predictive modeling, leading to improved accuracy and stronger generalization performance.

The analysis further revealed that the gradual increase in the number of features across scenarios significantly enhanced the predictive accuracy of the models. From Scenario 1 to Scenario 6, as the input space became richer, error indices (RMSE and MAE) consistently decreased, while the coefficient of determination (R^2) increased. This trend indicates that expanding the feature set enabled the models to capture more underlying data patterns, thereby improving predictive performance.

Among the tested algorithms, BR and LM benefited the most from the increase in feature dimensionality, achieving R^2 values greater than 0.90 from Scenario 3 onward. In contrast, GD was unable to leverage the additional features effectively and maintained poor accuracy throughout. RP followed a similar trend to LM and BR, though with slightly weaker performance.

In conclusion, considering both the impact of feature expansion and the comparative performance of the algorithms, the BR algorithm in Scenario 6 (maximum number of features) yielded the most accurate and stable results for estimating monthly radiation at the Kerman synoptic station, achieving an ARE of 4.5% and an R^2 value of 0.919 for the test dataset.

Figure 6 illustrates the comparison of test R^2 values obtained from FFNNs trained using different learning algorithms on the monthly scale. The results indicate that the LM and BR algorithms consistently achieve higher R^2 values across all scenarios, demonstrating superior predictive performance. In contrast, the GD algorithm exhibits significantly lower R^2 values, highlighting its limited convergence capability for this problem, while the RP algorithm shows competitive but slightly lower performance.

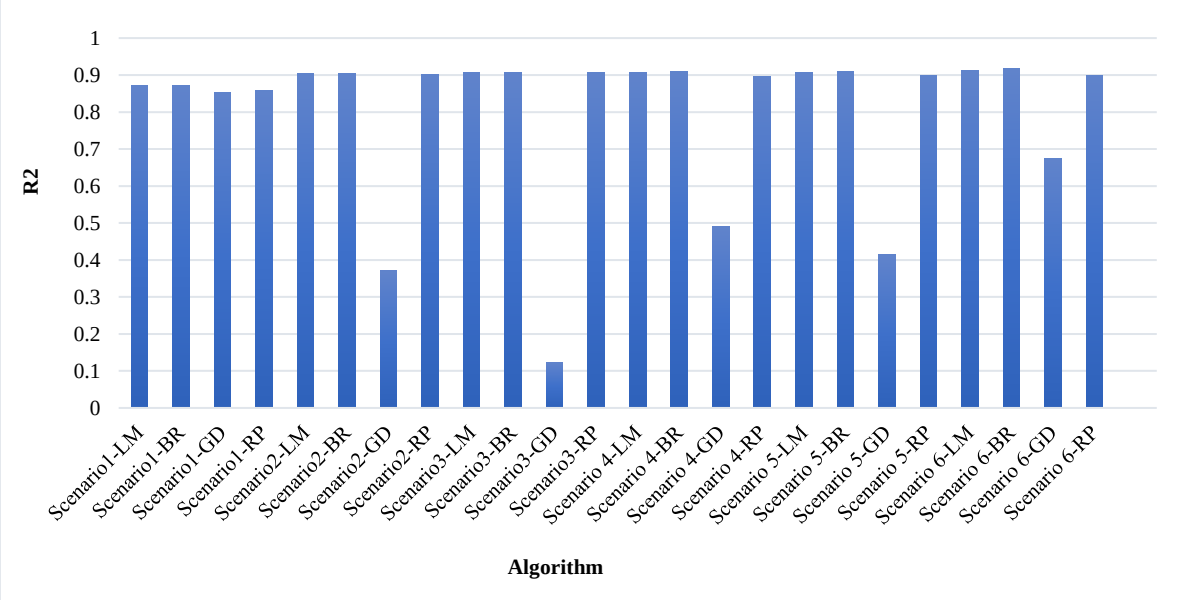

Fig. 6. Test R^2 values for FFNN models trained with different algorithms (LM, BR, GD, and RP) across monthly scenarios

Table 5 presents the results of the FFNNs on a daily scale. The results indicate that LM and BR generally achieve the best performance, consistently showing low RMSE and MAE values along with high R^2 across most scenarios. The BR outperforms LM in certain scenarios due to its regularization properties, which help prevent overfitting. RP demonstrates moderate performance, whereas GD exhibits the weakest performance, indicating its inability to effectively model complex data.

Regarding the scenarios, Scenario 6 delivers the best overall results, particularly for BR, which achieves the highest R^2 (0.899) and an ARE value of 2.66% for estimating daily radiation in the test dataset. Scenarios 2 and 5 also show excellent performance for both LM and BR, while Scenario 3 proves particularly challenging for GD. These scenario-dependent differences highlight the importance of considering data characteristics when selecting the most suitable learning algorithm.

Figure 7 further confirms that LM and BR consistently demonstrate superior predictive performance across most scenarios on the daily scale. Although RP shows reasonable performance in some scenarios, it generally underperforms compared to LM and BR, while GD exhibits substantial degradation, especially in Scenarios 3 and 5.

Table 5. Training error and testing error for FFNN on the daily scale

Information		Test					Train				
Scenario	Algorithm	RMSE	MAE	MBE	ARE	R^2	RMSE	MAE	MBE	ARE	R^2
1	LM	0.0324	0.0286	0.0283	4.3763	0.8172	0.0197	0.0159	-0.0039	2.2852	0.8464
	BR	0.0352	0.0316	0.0315	4.8451	0.816	0.0193	0.0159	-0.0014	2.2957	0.8485
	GD	0.0714	0.0604	0.0594	9.5134	0.8018	0.063	0.0518	0.0295	7.8709	0.8447
	RP	0.0349	0.0311	0.0311	4.7605	0.8116	0.0209	0.0175	0.0008	2.5481	0.824
2	LM	0.0318	0.0302	0.0302	4.6042	0.9159	0.0133	0.0106	-0.0031	1.5335	0.9314
	BR	0.0314	0.0297	0.0297	4.5371	0.9181	0.0134	0.0107	-0.0033	1.5539	0.9305
	GD	0.0931	0.0879	0.0879	13.6437	0.4656	0.0711	0.0577	0.0565	8.8611	0.7023
	RP	0.0309	0.0288	0.0288	4.3908	0.9053	0.0144	0.0113	-0.0023	1.6637	0.9170
3	LM	0.0366	0.035	0.035	5.3559	0.8993	0.0125	0.0098	-0.0003	1.4306	0.9355
	BR	0.0317	0.0303	0.0303	4.6264	0.9269	0.0131	0.0105	-0.0032	1.5222	0.9351
	GD	0.0745	0.0573	0.0529	8.9812	0.0013	0.0695	0.0596	0.0222	8.8349	0.0014
	RP	0.0376	0.0352	0.0352	5.3622	0.8662	0.0146	0.0118	-0.0017	1.7162	0.9142
4	LM	0.0298	0.028	0.028	4.2953	0.916	0.0132	0.0103	-0.0025	1.4822	0.9322
	BR	0.0303	0.0286	0.0286	4.3826	0.9164	0.0128	0.0102	-0.0026	1.4721	0.9365
	GD	0.0723	0.0585	-0.0267	8.8196	0.5796	0.1051	0.0888	-0.0497	12.5938	0.7756
	RP	0.0354	0.0327	0.0326	4.9927	0.8511	0.0152	0.0118	-0.0007	1.7344	0.9055
5	LM	0.0262	0.0239	0.0237	3.6477	0.9031	0.0131	0.0104	-0.0024	1.5185	0.9337
	BR	0.0258	0.0227	0.0223	3.5534	0.8645	0.0127	0.01	-0.0029	1.4423	0.937
	GD	0.055	0.0455	0.0439	7.1515	0.1023	0.0467	0.0407	0.0072	6.0116	0.1285
	RP	0.0254	0.0228	0.0226	3.4944	0.8889	0.0168	0.0136	-0.0028	1.9756	0.8871
6	LM	0.0262	0.0235	0.0235	3.5765	0.9025	0.0123	0.0096	0	1.3971	0.9381
	BR	0.0229	0.0176	0.0175	2.6646	0.8993	0.0098	0.0065	-0.0006	0.9633	0.961
	GD	0.0957	0.077	0.0709	12.1146	0.3595	0.0756	0.0627	0.0213	9.4259	0.2645
	RP	0.031	0.0269	0.0252	4.1016	0.7933	0.0155	0.0116	0.0002	1.6875	0.9098

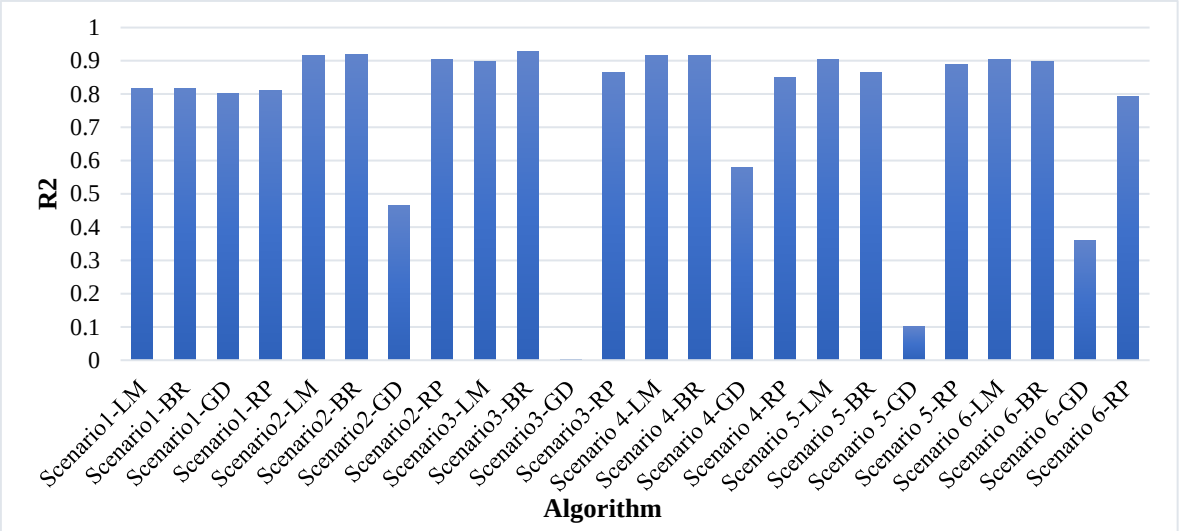

Fig. 7. Test R^2 values for FFNN models trained with different algorithms (LM, BR, GD, and RP) across daily scenarios

In summary, LM and BR on both monthly and daily scales are identified as the most recommended algorithms for FFNN-based modeling. GD, due to its poor performance, and RP, due to its relatively higher variability, are considered lower-priority options. These findings are consistent with previous studies, including Zhang and Behera (2012) and Bhuvaneswari *et al*. (2024), who highlighted the effectiveness of LM and BR algorithms for solar radiation estimation. The results further emphasize that careful consideration of learning algorithms and scenario configurations is essential for achieving high accuracy and reliable radiation predictions.

From a feature-based perspective, At the daily scale, FFNN performance is particularly sensitive to humidity-related variables such as SVP and MRH, which capture short-term atmospheric variability and cloud–moisture interactions that strongly influence daily solar radiation. In contrast, at the monthly scale, temporal aggregation smooths short-term fluctuations, and variables such as mean air temperature (MAT) and sunshine duration (n/N) become dominant contributors to model accuracy. This explains why scenarios with richer input features (Scenarios 5 and 6) consistently show higher and more stable R^2 values, especially when combined with LM and BR algorithms.

Overall, the impact of feature selection is scale-dependent, with daily predictions benefiting from moisture-related variables, while monthly predictions are more influenced by temperature and sunshine duration.

3.4 Comparison of scenarios in the LSTM networks

Examining Table 6 at the daily scale, the LSTM models exhibit ARE values ranging from 1.35% to 13.65% for the test dataset and R^2 values between 0.91 and 0.49 across the six scenarios. For the training dataset, ARE values range from 1.52% to 14.25 and R^2 values from 0.92 to 0.41. These results indicate that LSTM performance varies substantially depending on the scenario configuration. The consistently positive MBE values for the test dataset suggest a general tendency of the LSTM models to overestimate daily solar radiation.

A clear scenario-dependent pattern can be observed. Scenarios 1 to 5 demonstrate relatively stable and satisfactory performance, whereas Scenario 6 results in a pronounced degradation of

accuracy. In particular, Scenario 6 exhibits a sharp increase in ARE (13.65%) and a substantial drop in R^2 (0.49) for the test dataset, indicating poor generalization. This behavior suggests that, although LSTM models are capable of learning temporal dependencies effectively, they may become unstable when the input space becomes overly complex or contains redundant information.

Among all evaluated scenarios, Scenario 4 yields the most favorable results at the daily scale. In this scenario, the test dataset achieves an R^2 value of 0.91 and an ARE of 1.35%, while the training dataset shows similarly strong performance (R^2 = 0.92 and ARE = 1.52%). The close agreement between training and testing errors in Scenario 4 indicates good generalization and suggests that this scenario provides an optimal balance between input complexity and information relevance for LSTM modeling.

At the monthly scale (Table 7), a similar trend is observed. The LSTM models produce ARE values ranging from 5.10% to 12.37% for the test dataset and R^2 values between 0.89 and 0.56. Negative MBE values are observed in Scenarios 1 to 5, indicating a systematic underestimation of monthly solar radiation, whereas Scenario 6 shows a positive MBE, reflecting overestimation. Consistent with the daily-scale results, Scenario 6 exhibits markedly inferior performance, with a substantial increase in RMSE and ARE and a significant reduction in R^2, confirming that LSTM models are not suitable for monthly radiation estimation under this scenario.

Table 6. Training error and testing error for LSTM on the daily scale

Scenario	Test					Train				
	RMSE	MAE	MBE	ARE	R^2	RMSE	MAE	MBE	ARE	R^2
1	0.028058	0.0241	0.0237	3.73	0.8154	0.022934	0.0173	-0.01039	2.47	0.829
2	0.021411	0.0193	0.0189	2.96	0.9128	0.017056	0.0134	-0.00652	1.95	0.897
3	0.014093	0.0112	0.0060	1.73	0.8672	0.01907	0.0157	-0.00392	2.30	0.856
4	0.011021	0.0088	0.0032	1.35	0.9129	0.013837	0.0103	0.001759	1.52	0.922
5	0.013642	0.0100	0.0042	1.56	0.8638	0.016435	0.0120	-0.00305	1.74	0.895
6	0.009453	0.0761	0.0587	13.65	0.4896	0.009511	0.0789	0.04891	14.25	0.415

Table 7. Training error and testing error for LSTM on the monthly scale

Scenario	Test					Train				
	RMSE	MAE	MBE	ARE	R^2	RMSE	MAE	MBE	ARE	R^2
1	0.002258	0.0369	-0.0100	5.89	0.865	0.001985	0.034	-0.0004	5.734	0.875
2	0.001939	0.0332	-0.0104	5.51	0.886	0.001936	0.033	-0.001	5.635	0.878
3	0.001758	0.0321	-0.0096	5.19	0.896	0.00176	0.032	0.0021	5.442	0.889
4	0.001574	0.0318	-0.0173	5.10	0.899	0.001526	0.029	-0.001	4.962	0.904
5	0.001873	0.0331	-0.010	5.42	0.889	0.001638	0.030	0.0013	5.192	0.897
6	0.008192	0.0634	0.0257	12.37	0.565	0.008145	0.060	0.0271	12.300	0.559

Scenario 4 again provides the most reliable results at the monthly scale, achieving the highest R^2 (0.899) and the lowest ARE (5.10%) for the test dataset. Although Scenarios 1 to 5 show relatively small variations in R^2 (ranging from approximately 0.86 to 0.89), the superior balance between accuracy and stability observed in Scenario 4 highlights its robustness across temporal scales.

Overall, the scenario-based analysis demonstrates that LSTM models perform well in low- to moderate-dimensional input configurations, particularly in Scenario 4, where optimal accuracy and generalization are achieved at both daily and monthly scales. In contrast, the poor performance observed in Scenario 6 indicates that increasing feature dimensionality beyond a certain threshold can negatively affect LSTM stability and predictive capability. Additionally, MBE analysis reveals a scale-dependent bias, with a tendency toward overestimation at the daily scale and underestimation at the monthly scale in most scenarios.

The scenario-based behavior of LSTM models reveals a clear dependence on the relevance and dimensionality of input features. Scenarios 1 to 3 demonstrate that sunshine duration (n/N), combined with basic atmospheric moisture and temperature indicators (SVP and MAT), provides sufficient information for effective sequence learning. The optimal performance observed in Scenario 4 at both daily and monthly scales indicates that the inclusion of mean relative humidity (MRH) achieves a balanced representation of atmospheric moisture effects without introducing excessive redundancy.

In contrast, the substantial performance degradation observed in Scenario 6 suggests that the inclusion of numerous highly correlated meteorological variables (e.g., dew point temperature, wet bulb temperature, and vapor-related parameters) negatively affects LSTM stability. These variables convey overlapping physical information and increase input redundancy, leading to noise amplification and reduced generalization capability in sequence-based learning. Therefore, the LSTM results emphasize that moderate, physically relevant feature sets outperform high-dimensional configurations, highlighting Scenario 4 as the most suitable input structure for LSTM-based solar radiation estimation.

3.5 Comparison of FFNN and LSTM on Monthly Scale

A detailed comparison of FFNN and LSTM models on the monthly scale was conducted using the results presented in Tables 4 and 7 along with Figure 8. In Scenario 1, both FFNN (particularly LM and BR algorithms) and LSTM showed acceptable performance. FFNN-LM and FFNN-BR achieved RMSE values of approximately 0.0020 and 0.0021, respectively, whereas LSTM's RMSE was slightly higher at 0.00225. Similarly, the R^2 values for FFNN-LM/BR were slightly above 0.87, while LSTM reached 0.865. Although differences are minor, FFNN-LM/BR slightly outperformed LSTM in both accuracy and stability.

In Scenario 2, FFNN-LM/BR continued to exhibit superior performance. The RMSE for FFNN-LM/BR decreased to about 0.0015, while LSTM's RMSE remained higher at 0.001939. R^2 values for FFNN-LM/BR exceeded 0.90, whereas LSTM was 0.886. This indicates that LSTM did not benefit as effectively from the increased number of input features as FFNN-LM/BR. FFNN-RP also performed well (RMSE ≈ 0.0016, $R^2 \approx 0.90$), whereas FFNN-GD failed to provide reliable predictions.

Scenario 3 showed a slight widening of performance gaps. FFNN-LM/BR and RP maintained RMSE values around 0.0015 with R^2 approximately 0.906, while LSTM had RMSE near 0.00176 and R^2 about 0.896. Despite small differences, FFNN-LM/BR delivered more precise and stable predictions.

In Scenario 4, FFNN-BR achieved the best overall results with RMSE of 0.0014, R^2 of 0.9107, and ARE of 4.84% for the test dataset, while LSTM slightly lagged behind (RMSE = 0.001574, $R^2 = 0.899$, ARE = 5.10%). Scenario 5 further emphasized the advantage of FFNN-LM/BR, as LSTM's RMSE increased to 0.001873 and R^2 dropped to 0.889, whereas FFNN-LM/BR maintained RMSE around 0.0014–0.0015 and R^2 above 0.90.

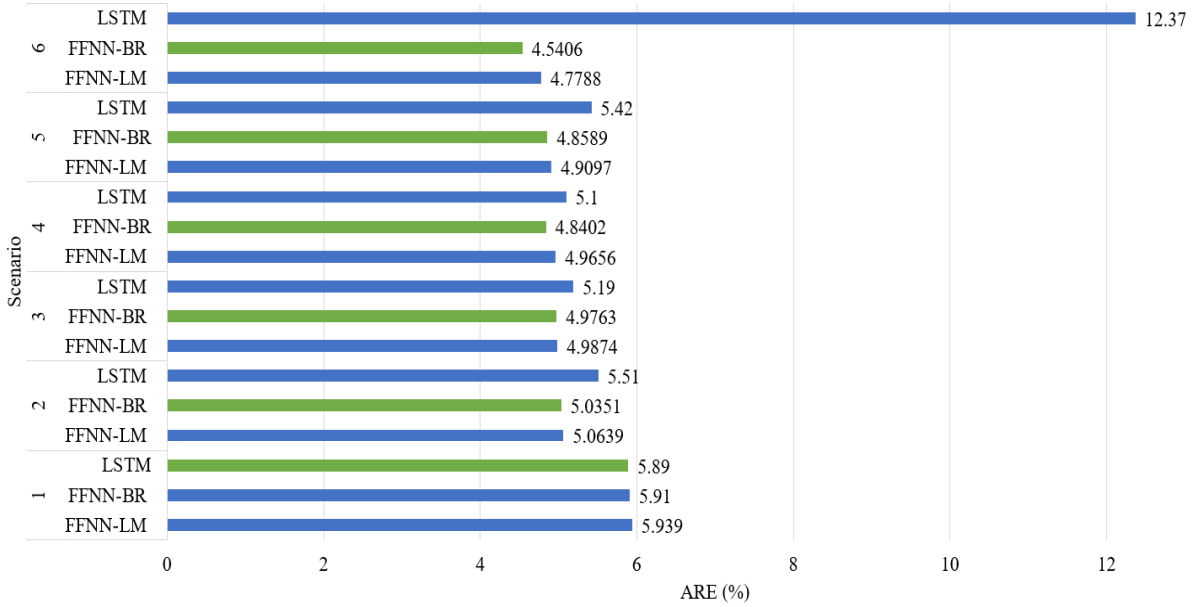

Fig. 8. ARE values for each scenario for FFNN-LM, FFNN-BR, and LSTM on monthly scale

Finally, Scenario 6 highlighted a substantial difference between the two models. LSTM performance deteriorated dramatically, with RMSE rising to 0.008192 and R^2 declining to 0.565, indicating instability and poor generalization in high-dimensional settings. In contrast, FFNN-LM/BR maintained high stability, with RMSE around 0.0013–0.0015 and R^2 near 0.919. FFNN-RP also performed well (RMSE ≈ 0.0016, R^2 ≈ 0.8988), significantly outperforming LSTM.

Overall, FFNN-LM/BR consistently achieved better accuracy and stability across most monthly scenarios, especially in complex or high-dimensional settings. LSTM performed reasonably in low to medium-dimensional scenarios but failed to maintain predictive accuracy in Scenario 6. Therefore, for monthly solar radiation estimation, FFNN-BR under Scenario 6 emerges as the optimal model, achieving ARE of 4.54% and R^2 of 0.919, demonstrating both robustness and precision.

3.6 Comparison of FFNN and LSTM on daily scale

The comparison on a daily scale was performed using Tables 5 and 6 along with Figure 9. Scenario 1 indicated that FFNN-LM/BR and LSTM performed similarly. FFNN-LM/BR reached R^2 values of about 0.817, while LSTM achieved slightly lower RMSE, indicating a minor advantage in error terms for LSTM.

In Scenario 2, LSTM outperformed FFNN in terms of RMSE (0.021 vs. ~0.031), though R^2 values remained comparable. Scenario 3 presented a nuanced result: LSTM achieved the lowest errors (RMSE = 0.014, MAE = 0.011), but R^2 dropped to 0.867, lower than FFNN-BR (R^2 = 0.927). This suggests that LSTM better minimized prediction errors, whereas FFNN-BR more accurately captured overall data variability.

Scenario 4 demonstrated strong performance for both models. LSTM had lower RMSE and MAE (0.011 and 0.0088, respectively), while FFNN-LM/BR maintained R^2 around 0.91, indicating comparable explanatory power. Scenario 5 emphasized the advantage of FFNN-LM/BR in high-dimensional scenarios, as LSTM's error slightly increased, though it still showed reasonable predictions.

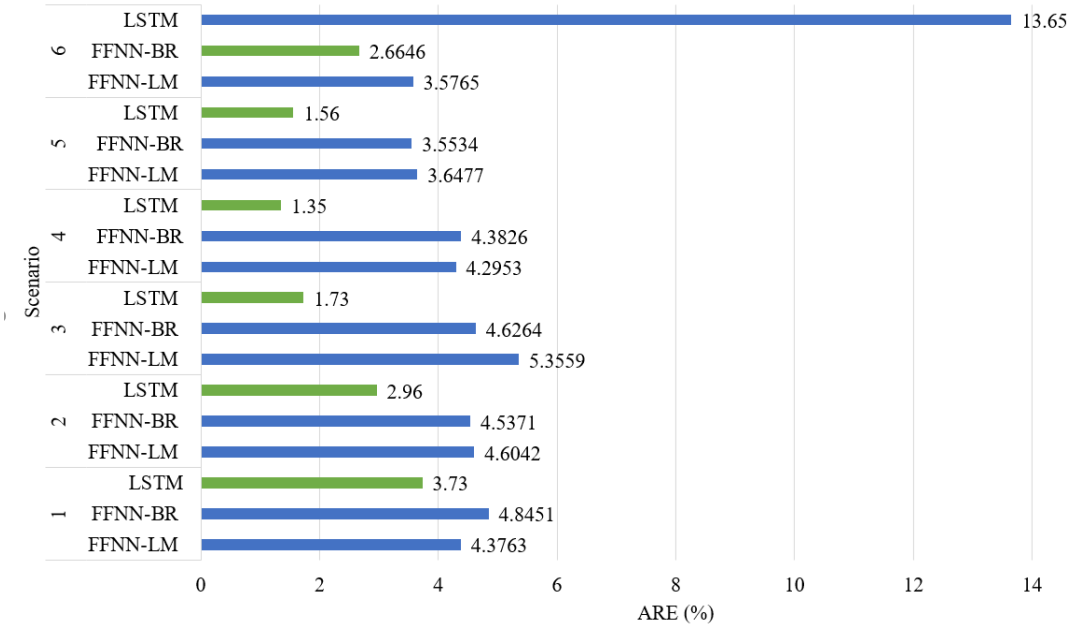

Fig. 9. ARE values for each scenario for FFNN-LM, FFNN-BR, and LSTM on daily scale

Scenario 6 revealed the limitations of LSTM in complex, high-dimensional daily data. Despite an RMSE of 0.009453, MAE and R^2 indicated significant discrepancies between training and test datasets ($R^2 = 0.4896$), suggesting overfitting or unstable learning. Conversely, FFNN-LM/BR maintained excellent performance ($R^2 \approx 0.91$, RMSE $\approx$ 0.0014–0.0016), demonstrating superior generalization and robustness. FFNN-RP also performed reliably ($R^2 \approx$ 0.8988, RMSE $\approx$ 0.0016), far surpassing LSTM.

In summary, LSTM models are effective for estimating daily solar radiation in low to medium-dimensional scenarios, providing precise short-term forecasts and capturing rapid variations. However, in high-dimensional or complex scenarios, FFNN-LM/BR are more stable, accurate, and reliable. These results indicate that model selection should consider both data resolution and feature complexity to maximize predictive performance.

A consolidated comparison between the best-performing FFNN models (LM and BR) and LSTM across all scenarios highlights scenario-dependent strengths and limitations. On both daily and monthly scales, FFNN-LM/BR consistently demonstrates high accuracy and stability, particularly in high-dimensional scenarios (Scenarios 5 and 6), where the richer input feature sets allow these models to capture complex nonlinear relationships effectively. LSTM models, however, perform well in low- to medium-dimensional scenarios (Scenarios 1–4), benefiting from their ability to learn temporal dependencies, but show instability and reduced generalization in Scenario 6 due to over-complexity and potential feature redundancy. These observations indicate that FFNN-LM/BR are more robust when handling large feature spaces, whereas LSTM is suitable for capturing short-term temporal patterns in simpler or moderate input configurations. Overall, scenario-specific model selection is recommended: FFNN-LM/BR for high-dimensional or complex data, and LSTM for low- to medium-dimensional time-series prediction tasks.

Despite the positive outcomes of this study, several critical limitations should be acknowledged as directions for future research. First, this study is limited to an arid and semi-

arid region, and the results may differ in other climatic conditions. Second, the dataset utilized was limited to a few meteorological variables; incorporating more comprehensive datasets, including additional atmospheric parameters, altitude, and satellite-derived data, could enhance predictive accuracy. Third, the focus on FFNN and LSTM models precludes assessment of other advanced deep learning algorithms and hybrid approaches, which may further improve performance. Moreover, the analysis was conducted only at daily and monthly time scales; exploring shorter or longer scales (hourly, seasonal, annual) could provide a more holistic understanding of model behavior. Finally, employing optimization techniques and feature selection strategies can reduce input complexity while boosting model accuracy and efficiency. Additionally, a variety of learning algorithms, such as BFGS Quasi-Newton, Scaled Conjugate Gradient, Conjugate Gradient with Powell/Beale Restarts, Fletcher-Powell Conjugate Gradient, Polak-Ribiére Conjugate Gradient, One Step Secant, Variable Learning Rate Gradient Descent, and Gradient Descent with Momentum, can also be effectively employed for FFNN training, further broadening the scope for future studies.

4. Conclusions

Solar radiation estimation plays a vital role in various fields, including energy production, architecture, health, and agriculture. In agriculture, it aids in assessing plant light requirements, irrigation planning, crop selection, optimizing crop performance, and weather forecasting. Consequently, it serves as a powerful tool for enhancing productivity and performance in the agricultural sector. The accuracy of radiation estimates in different scientific disciplines related to this essential parameter can be improved by collecting comprehensive and precise solar radiation data and addressing any statistical gaps.

The objective of this research is to enhance the accuracy of solar radiation estimation. Despite the complexity of meteorological variables, there exist varying correlations among different weather parameters, which depend on the influences and interactions between these variables. Initially, the correlation between meteorological variables and radiation was calculated at both monthly and daily scales. Variables exhibiting high correlations were selected for modeling purposes. FFNN models were then trained using the chosen meteorological variables and various learning algorithms such as LM, BR, GD, and RP to estimate solar radiation under six different scenarios. LSTM network models were developed under similar scenarios. The performance of the models was evaluated using error evaluation criteria such as RMSE, MAE, ARE, MBE, and R^2 at both daily and monthly scales.

The research findings indicate that the LSTM model, under scenario 4, utilizing inputs including the sunshine hours fraction, saturated vapor pressure, mean daily temperature, and mean relative humidity, with the Adam algorithm, yields the best results for estimating daily radiation. It achieves an R^2 of 0.91 for the test dataset and an ARE of 1.35%. On a monthly scale, the FFNN model, under scenario 6, employing the BR algorithm, demonstrates the highest performance for estimating the radiation variable. It achieves an R^2 of 0.92, and an ARE of 4.5% for the test dataset. Overall, the use of ANNs provides more precise estimations of radiation data in both short-term and long-term time scales compared to deep learning networks. Furthermore, the comparison of learning algorithms highlights the significant influence of ANN structure on the accuracy of model training. Therefore, conducting further research to evaluate the performance of different ANNs with varying structures in radiation estimation is imperative. By doing so, the accuracy and reliability of radiation data can be enhanced.

Nomenclature

ANN	Artificial Neural Network
FFNN	Feed-Forward Neural Network
LSTM	Long Short-Term Memory
GD	Gradient Descent Learning Algorithm
BR	Bayesian Regularization Learning Algorithm
RP	Resilient Propagation Learning Algorithm
LM	Levenberg–Marquardt Learning Algorithm
R_S	observed solar radiation (W/m^2)
R_{cd}	daily clear sky radiation (W/m2)
R_0	extraterrestrial daily radiation (W/m^2)
N_n	sunshine hours fraction
SVP	Saturated Vapor Pressure (mb)
MAT	Mean Air Temperature (°C)
MRH	Mean Relative Humidity (%)
MST	Mean Soil Temperature (°C)
HV	Horizontal Visibility (m)
MW	Mean Wind speed (m/s)
DP	Dew Point temperature (°C)
WB	Wet Bulb temperature (°C)
P	Pressure (mb)
C	Cloudiness (Okta)
MAE	Mean Absolute Error
RMSE	Root Mean Squared Error
MBE	Mean Bias Error
R^2	R-square

Authors' contribution

S. Mohtashami: Gathering the experimental data, Data curation, Software; Methodology; Conceptualization, Methodology, Writing-Reviewing and Editing, Investigation, Formal analysis, Analyzing the experimental data, Writing-Original draft preparation *Z. Aghashariatmadari: Supervision, Investigation, Conceptualization, Methodology, Analyzing the experimental data, Validation, Visualization, , Reviewing and Editing. All authors have read and agreed to the published version of the manuscript.

Data availability

Data available on request from the author.

Acknowledgements

The research was supported by the University of Tehran. The authors would like to express their special thanks to the vice chancellor for research affairs.

Ethical considerations
The author avoided data fabrication, falsification, plagiarism, and misconduct

Funding
This research did not receive any specific grant from funding agencies in the public, commercial, or not-for-profit sectors.

Conflict of interest
The authors declare no conflict of interest.

References

Abdulazeez, M. A. (2011). Artificial neural network estimation of global solar radiation using meteorological parameters in Gusau, Nigeria. *Archives of Applied Science Research, 3*(2), 586–595.

Abraha, M. G., & Savage, M. J. (2008). Comparison of estimates of daily solar radiation from air temperature range for application in crop simulations. *Agricultural and Forest Meteorology, 148*(3), 401–416. https://doi.org/10.1016/j.agrformet.2007.10.001

Adam, A., Zheng, Y., & Hamad, A. (2025). Solar Radiation Prediction in Semi-Arid Regions: A Machine Learning Approach and Comprehensive Evaluation in Gadarif, Sudan. *Italian Journal of Agrometeorology*. https://doi.org/10.36253/ijam-2815

Afshari Pour, S., Hamzeh, S., & Neysani Samany, N. (2017). Site selection of solar power plant using GIS-Fuzzy DEMATEL model: A case study of Bam and Jiroft cities of Kerman Province in Iran. *Journal of Solar Energy Research, 2*(4), 323–328.

Arseven, B., & Çınar, S. M. (2025). A novel hybrid solar radiation forecasting algorithm based on discrete wavelet transform and multivariate machine learning models integrated with clearness index clusters. *Journal of Atmospheric and Solar-Terrestrial Physics*, 267, 106417. https://doi.org/10.1016/j.jastp.2025.106417

Asaf, D., Rotenberg, E., Tatarinov, F., Dicken, U., Montzka, S. A., & Yakir, D. (2013). Ecosystem photosynthesis inferred from measurements of carbonyl sulphide flux. *Nature Geoscience, 6*(3), 186–190. https://doi.org/10.1038/ngeo1730

Attya, M., Abo-Seida, O., Abdulkader, H., & Monir, A. (2025). Advanced solar radiation prediction using combined satellite imagery and tabular data processing. *Scientific Reports, 15,* 96109. https://doi.org/10.1038/s41598-025-96109-0

Benesty, J., Chen, J., & Huang, Y. (2008). On the importance of the Pearson correlation coefficient in noise reduction. *IEEE Transactions on Audio, Speech, and Language Processing, 16*(4), 757–765. https://doi.org/10.1109/TASL.2008.919072

Benkaciali, S., Notton, G., & Voyant, C. (2025). Comparative study of feature selection techniques for machine learning-based solar irradiation forecasting to facilitate the sustainable development of photovoltaics: Application to Algerian climatic conditions. *Sustainability*, *17*(14), 6400. https://doi.org/10.3390/su17146400

Besharat, F., Dehghan, A. A., & Faghih, A. R. (2013). Empirical models for estimating global solar radiation: A review and case study. *Renewable and Sustainable Energy Reviews, 21,* 798–821. https://doi.org/10.1016/j.rser.2012.12.043

Bhuvaneswari, M., Prasanna Kumar, T. J., Gobikrishnan, U., Rajesh, S., Antony Prabu, D., & Seenivasan, M. (2024). Solar radiation forecast utilizing an artificial neural network model with three distinct learning algorithms. *SAE Technical Paper 2023-01-5174.* https://doi.org/10.4271/2023-01-5174

Bian, Z., Chong, W., Ding, L., & Yang, W. (2019). Analysis and research on quality control method of global radiation observation data. *The Journal of Engineering, 23,* 8975–8979. https://doi.org/10.1049/joe.2018.9161

Bohat, V. K., & Arya, K. V. (2018). An effective gbest-guided gravitational search algorithm for real-parameter optimization and its application in training of feedforward neural networks. *Knowledge-Based Systems, 143,* 192–207. https://doi.org/10.1016/j.knosys.2017.12.011

Bouat, K., Othman, A., & Besbes, M. (2018). Estimation of global and direct solar radiation in Tunisia based on geostationary satellite imagery. In *IEEE PES/IAS PowerAfrica* (pp. 190–194). https://doi.org/10.1109/PowerAfrica.2018.8521155

Camacho, E. F., Berenguel, M., Rubio, F. R., & Martínez, D. (2012). *Control of solar energy systems.* Springer. https://doi.org/10.1007/978-0-85729-916-1

Çelik, Ö., Teke, A., & Yıldırım, H. B. (2016). The optimized artificial neural network model with Levenberg–Marquardt algorithm for global solar radiation estimation in Eastern Mediterranean region of Turkey. *Journal of Cleaner Production, 116,* 1–12. https://doi.org/10.1016/j.jclepro.2015.12.082

Cervantes, I., Cervantes-Ortiz, C. A., Vazquez-Santana, D.-H., & Arguelles, A. (2025). Heuristic-machine learning models for solar radiation forecasting in Köppen climate zones. *Applied Soft Computing,* 171, 112807. https://doi.org/10.1016/j.asoc.2025.112807

Chauhan, R., Sharma, S., & Pachauri, R. (2024). Performance prediction of conventional and modified solar stills using Levenberg Marquardt algorithm-based artificial neural network model: An experimental and stochastic evaluation. *Journal of Solar Energy Research, 9*(3), 1966–1980. https://doi.org/10.22059/jser.2024.380006.1449

Demir, V. (2025). Evaluation of solar radiation prediction models using AI: A performance comparison in the high-potential region of Konya, *Türkiye. Atmosphere, 16*(4), 398. https://doi.org/10.3390/atmos16040398

Edelmann, D., Mori, T. F., & Szekely, G. J. (2021). On relationships between the Pearson and the distance correlation coefficients. *Statistics & Probability Letters*. https://doi.org/10.1016/j.spl.2020.108960

Ertekin, C., & Yaldız, O. (1999). Estimation of monthly average daily global radiation on horizontal surface for Antalya (Turkey). *Renewable Energy, 17*(1), 95–102. https://doi.org/10.1016/s0960-1481(98)00109-8

Fischer, T., & Krauss, C. (2018). Deep learning with long-term memory networks for financial market predictions. *European Journal of Operational Research*. FAU Discussion Papers in Economics. https://doi.org/10.1016/j.ejor.2017.11.054.

Fraihat, H., Almbaideen, A. A., Al-Odienat, A., Al-Naami, B., De, Fazio, R., & Visconti, P. (2022). Solar radiation forecasting by Pearson correlation using LSTM neural network and ANFIS method: Application in the West-Central Jordan. *Future Internet, 14*, 79. https://doi.org/10.3390/fi14030079

Ghaffarzadeh, N., & Azadian, A. (2019). A comprehensive review and performance evaluation in solar (PV) systems fault classification and fault detection techniques. *Journal of Solar Energy Research, 4*(4), 252–272. https://doi.org/10.22059/jser.2019.289072.1127

Gueymard, C.A., & Myers, D.R. (2008). Validation and ranking methodologies for solar radiation models. In *Modeling Solar Radiation at the Earth's Surface* (pp. 479–481). Springer, Berlin, Germany. https://doi.org/10.1007/978-3-540-77455-6_20

Gürel, A. E., Ağbulut, Ü., Bakır, H., Ergün, A., & Yıldız, G. (2023). A state of art review on estimation of solar radiation with various models. *Heliyon*, 9(2), e13167. https://doi.org/10.1016/j.heliyon.2023.e13167

Hari, N. B. S., & Subbulekshmi, D. (2022). Performance analysis of FFBP-LM-ANN based hourly GHI prediction using environmental variables: A case study in Chennai. *Mathematical Problems in Engineering, 2022*, 1–12. https://doi.org/10.1155/2022/1713657

Heaton, J. (2008). *Introduction to neural networks with Java* (pp. 26–29). Heaton Research.

Hochreiter, S., & Schmidhuber, J. (1997). Long short-term memory. *Neural Computation, 9*, 1735–1780. https://doi.org/10.1162/neco.1997.9.8.1735

James, T. O., Gulumbe, S. U., & Danbaba, A. (2018). Resilient back-propagation algorithm in the prediction of mother to Child transmission of HIV. *Open Access Library Journal, 5*, 1–7. https://doi.org/10.4236/oalib.1104538

Jazayeri, K., Jazayeri, M., & Uysal, S. (2016). Comparative analysis of Levenberg–Marquardt and Bayesian regularization backpropagation algorithms in photovoltaic power estimation using artificial neural network. In L. Cheng, A. C. S. Leung, & S. Ozawa (Eds.), *Neural information processing* (Vol. 9728, pp. 80–95). Springer. https://doi.org/10.1007/978-3-319-41561-1_7

Jebli, I., Belouadha, F. Z., Kabbaj, M. I., & Tilioua, A. (2021). Prediction of solar energy guided by Pearson correlation using machine learning. *Energy, 224*, 120109. https://doi.org/10.1016/j.energy.2021.120109

Kusuma, H., Three, U., Suprianto, B., & Firmansyah, R. (2025). Short-term solar radiation forecasting for adaptive solar cell using a hybrid D-FFNN model. *Journal of Energy Research and Reviews*, 17, 24–41. https://doi.org/10.9734/jenrr/2025/v17i2395

Lauret, P., David, M., Fock, E., Bastide, A., & Riviere, C. (2006). Bayesian and sensitivity analysis approaches to modeling the direct solar irradiance. *Journal of Solar Energy Engineering, 128*(3), 394–405. https://doi.org/10.1115/1.2210495

Malik, P., Malik, P., Gehlot, A., & Singh, R. (2023). Prediction of wind speed and solar radiation using LM and BR neural network algorithm. *AIP Conference Proceedings*, 020018. https://doi.org/10.1063/5.0152368

Mazorra Aguiar, L., Pereira, B., David, M., Díaz, F., & Lauret, P. (2015). Use of satellite data to improve solar radiation forecasting with bayesian artificial neural networks. *Solar Energy, 122*, 1309–1324. https://doi.org/10.1016/j.solener.2015.10.041

Meenal, R., & Selvakumar, A. I. (2017). Review on artificial neural network based solar radiation prediction. In *Proceedings of the 2nd International Conference on Communication and Electronics Systems (ICCES)* (pp. 302–305). Coimbatore, India. https://doi.org/10.1109/CESYS.2017.8321285

Moradi, I. (2009). Quality control of global solar radiation using sunshine duration hours. *Energy, 34*, 1–6. https://doi.org/10.1016/j.energy.2008.09.006

Moshkbar-Bakhshayesh, K. (2019). Development of a modular system for estimating attenuation coefficient of gamma radiation: Comparative study of different learning algorithms of cascade feedforward neural network. *Journal of Instrumentation, 14*(10), P10010. https://doi.org/10.1088/1748-0221/14/10/p10010

Moshkbar-Bakhshayesh, K. (2021). The ensemble approach in comparison with the diverse feature selection techniques for estimating NPPs parameters using the different learning algorithms of the feedforward neural network. *Nuclear Engineering and Technology, 53*(12), 3944–3951. https://doi.org/10.1016/j.net.2021.06.030

Okut, H. (2016). Bayesian regularized neural networks for small n big p data. In *Artificial neural networks—Models and applications*. IntechOpen. https://doi.org/10.5772/63256

Oliveira, M., Silva Lopes, H., Mendonça, P., Tenpierik, M., & Silva, L. T. (2024). Solar radiation measurement tools and their impact on in situ testing—A Portuguese case study. *Buildings*, 14(7), 2117. https://doi.org/10.3390/buildings14072117

Pan, B., Yu, H., Cheng, H., Du, S., Cai, S., & Zhao, M. (2023). A CNN–LSTM machine-learning method for estimating particulate organic carbon from remote sensing in lakes. *Sustainability, 15*(17), 13043. https://doi.org/10.3390/su151713043

Qazi, A., Fayaz, H., & Wadi, A. (2015). The artificial neural network for solar radiation prediction and designing solar systems: A systematic literature review. *Journal of Cleaner Production, 104*, 1–12. https://doi.org/10.1016/j.jclepro.2015.04.041

Rai, A., Shrivastava, A., Jana, K. C., Liu, J., Singh, K., Jayalakshmi, N. S., & Agrawal, A. (2025). Meta-machine learning framework for robust short-term solar power prediction across different climatic zones. *Engineering Applications of Artificial Intelligence*, 147, 110295. https://doi.org/10.1016/j.engappai.2025.110295

Reddy, L. R., Patel, P., & Rajendra, S. K. (2020). Utilization of resilient back propagation algorithm and discrete wavelet transform for the differential protection of three phase power transformer. In *21st National Power Systems Conference (NPSC)*. https://doi.org/10.1109/npsc49263.2020.9331861

Shamshirband, S., Mohammadi, K., Chen, H.L., Samy, G.N., Petković, D., & Ma, C. (2015). Daily global solar radiation prediction from air temperatures using kernel extreme learning machine: A case study for Iran. *Journal of Atmospheric and Solar-Terrestrial Physics, 134*, 109–117. https://doi.org/10.1016/j.jastp.2015.09.014

Tasie, N., Israel-Cookey, C., & Banyie, L. (2018). The effect of relative humidity on the solar radiation intensity in Port Harcourt, Nigeria. *International Journal of Research, 5*, 128–136.

Tazik, E., Rezaei, A., Abkar, A., Alavipanaha, K., Jahantab, Z., & Rahmati, A. (2017). Estimation of daily global solar radiation using MODIS data for a clear sky day (case study: northwest of Iran). *Journal of Solar Energy Research, 2*(3), 33–38.

Tilahun, F. B. (2024). Fuzzy-based predictive deep reinforcement learning for robust and constrained optimal control of industrial solar thermal plants. *Applied Soft Computing*, 159, 111432. https://doi.org/10.1016/j.asoc.2024.111432

Venkata Teja, U., Sai Kiran, M., Karthikeya, V., Murali, E., & Kumanan, T. (2025). Solar radiation prediction using machine learning and Python. *International Journal on Science and Technology*, 16(1), 1-10. https://doi.org/10.71097/IJSAT.v16.i1.2713

Waewsak, J., Chancham, C., Mani, M., & Gagnon, Y. (2014). Estimation of monthly mean daily global solar radiation over Bangkok, Thailand using artificial neural networks. *Energy Procedia, 57*, 1160–1168. https://doi.org/10.1016/j.egypro.2014.10.103

Wang, Z., Peng, T., Zhang, X., Chen, J., Qian, S., & Zhang, C. (2025). Enhancing multi-step short-term solar radiation forecasting based on optimized generalized regularized extreme learning machine and multi-scale Gaussian data augmentation technique. *Applied Energy*, 377, 124708. https://doi.org/10.1016/j.apenergy.2024.124708

Wild, M. (2009). Global dimming and brightening: A review. *Journal of Geophysical Research, 114.* https://doi.org/10.1029/2008JD011470

Yacef, R., Benghanem, M., & Mellit, A. (2012). Prediction of daily global solar irradiation data using Bayesian neural network: A comparative study. *Renewable Energy, 48*, 146–154. https://doi.org/10.1016/j.renene.2012.04.036

Yadav, A. K., & Chandel, S. S. (2014). Solar radiation prediction using artificial neural network techniques: A review. *Renewable and Sustainable Energy Reviews, 33*, 772–781. https://doi.org/10.1016/j.rser.2013.08.055

Yadav, A., Kumar, R., Wang, M., Fekete, G., & Singh, T. (2025). Comparative analysis of daily global solar radiation prediction using deep learning models inputted with stochastic variables. *Scientific Reports*, 15. https://doi.org/10.1038/s41598-025-95281-7

Yan, Z., Lu, X., Wu, L., Zhang, H., Liu, F., Wang, X., Xu, W., & Liu, W. (2025). Enhancing short-term solar radiation forecasting with hybrid VMD and GraphCast-based machine learning models. *Expert Systems with Applications*, 285, 128042. https://doi.org/10.1016/j.eswa.2025.128042

Yang, F., Gao, P., & Lu, Y. (2016). Evolving resilient back-propagation algorithm for energy efficiency problem. *MATEC Web of Conferences*, *77*, 06016. https://doi.org/10.1051/matecconf/20167706016

Zeng, J., & Qiao, W. (2011). Short-term solar power prediction using an RBF neural network. In *Proceedings of the IEEE Power and Energy Society General Meeting* (pp. 1–8). Detroit, MI, USA. https://doi.org/10.1109/PES.2011.6039204

Zerouali, B., Bailek, N., Qaysi, S., Difi, S., Alarifi, N., Elbeltagi, A., Santos, C. A. G., He, K., & Youssef, Y. M. (2025). Hybrid machine learning optimization for solar radiation forecasting. *Physics and Chemistry of the Earth*, 140, 104052. https://doi.org/10.1016/j.pce.2025.104052

Zhang, N., & Behera, P. K. (2012). Solar radiation prediction based on recurrent neural networks trained by Levenberg–Marquardt backpropagation learning algorithm. In *2012 IEEE PES Innovative Smart Grid Technologies (ISGT)* (pp. 1–7). IEEE. https://doi.org/10.1109/ISGT.2012.6175757